Electronic Supplementary Information

Defective Nanoporous Zinc Cobaltite as Potential Bifunctional Oxygen Electrocatalyst

Gowra Raghupathy Dillip[#†], Gundegowda Kalligowdanadoddi Kiran[$†], Abhishek Bharti[$], Tanmay Mohan Bhagwat[&], Gopalakrishnan Sai Gautam[&*], and Aninda J. Bhattacharyya[$,*]

[#]*Energy Institute, Centre of Rajiv Gandhi Institute of Petroleum Technology, Bengaluru, 560064 India*

[$]*Solid State and Structural Chemistry Unit, Indian Institute of Science, Bengaluru, 560012, India*

[&]*Department of Materials Engineering, Indian Institute of Science, Bengaluru, 560012, India*

† GRD and GKK contributed equally.

Corresponding Authors: anindajb@iisc.ac.in and saigautamg@iisc.ac.in

Characterization

The crystal structure of zinc cobaltite (ZCO) was identified by an X-ray diffractometer (PANalytical X'Pert Pro, USA) with Cu Kα (λ = 0.154 nm) at 40 kV and 30 mA. The data were used to refine the X-ray diffraction (XRD) structures using the Rietveld method to quantify the Zn, Co, and O occupancies in both samples. The XPert Highscore Plus 3.0 Commercial software was used to perform the refinement. The sample's microstructure was inspected by field-emission scanning electron microscopy (FESEM, S-4800, Hitachi, Japan) and high-resolution transmission electron microscopy (HRTEM, Tecnai G2 F20 S-Twin, USA) with a field emission gun in Schottky mode at 200 kV. The surface states of samples were compared using an X-ray Photoelectron Spectrometer (XPS, K-alpha, Thermo Scientific, USA) with source Al Kα energies of 1486.6 eV. The charge corrections were done by referring the spectra to standard carbon, C 1s binding energy 286.8 eV. Surface area measurements were recorded on a surface analyzer (3-Flex, Micromeritics, USA). A potentiostat/galvanostat was attached to the automatic motor-controlled rotating disk electrode setup (Multi Autolab 204, Metrohm) in bipotentiostat mode for electrochemical measurements.

Electrocatalytic Activity

The electrode potential is converted from Ag/AgCl scale to the reference hydrogen electrode (RHE) scale via the Nernst equation using the following formula:[1]

$$E_{RHE} = E_{Ag/AgCl} + 0.059\ \text{pH} + E^0_{Ag/AgCl} \quad \text{(s1)}$$

where,

$$E^0_{Ag/AgCl} = 0.197\ V \quad \text{(s2)}$$

The electron transfer number (n) of the oxygen reduction reaction (ORR) is determined from the Koutecky–Levich (K-L) plot using the K-L equation as follows:

$$\frac{1}{j} = \frac{1}{j_K} + \frac{1}{j_L} = \frac{1}{j_K} + \frac{1}{B\omega^{1/2}} \quad \text{(s3)}$$

$$B = 0.62nFC_0D_0^{2/3}\vartheta^{-1/6} \quad \text{(s4)}$$

$$j_K = nFKC_0 \quad \text{(s5)}$$

where j, j_K, and j_L are the measured, kinetic and diffusion-limiting current densities in mA/cm^2, respectively, n is the electron transfer number, ω is the angular velocity of the rotating ring disk electrode (RRDE; $\omega = 2\pi N$, where N is the linear rotation speed in rpm), F is the Faraday's constant (96485 C mol^{-1}), C_0 is the bulk concentration of O_2 (1.2 x 10^{-6} mol cm^3), D_0 is the diffusion coefficient of O_2 in 0.1 KOH (1.9 x 10^{-5} cm^2 s^{-1}), ϑ is the kinetic viscosity of the electrolyte (0.01 cm^2 s^{-1}), K is the electron transfer rate constant. Using the above equation, n can be estimated from the slope of a linear fit of K-L plots.

Using the RRDE data of ORR, the electron transfer number and H_2O_2 % were calculated using the following equations:[2]

$$n = 4 \times \frac{I_D}{I_D + \frac{I_R}{N}} \quad \text{(s6)}$$

$$H_2O_2\% = 200 \times \frac{\frac{I_R}{N}}{I_D + \frac{I_R}{N}} \quad \text{(s7)}$$

I_D and I_R are the disk and ring currents, respectively, and N is the collection efficiency of the ring electrode (0.249). The electrochemical active surface area (ECSA) of the samples was estimated from the cyclic voltammetry (CV) of the samples in a non-faradaic region using the following equation:

$$ECSA = \frac{C_{dl}}{C_s} \quad \text{(s8)}$$

C_{dl} = non-faradaic double-layer capacitance from CV curves (in mF), and C_s = general specific capacitance (mF cm^{-2}), taken as 0.04 mF cm^{-2} from a previous report on metal electrodes in aqueous KOH electrolytes.[3]

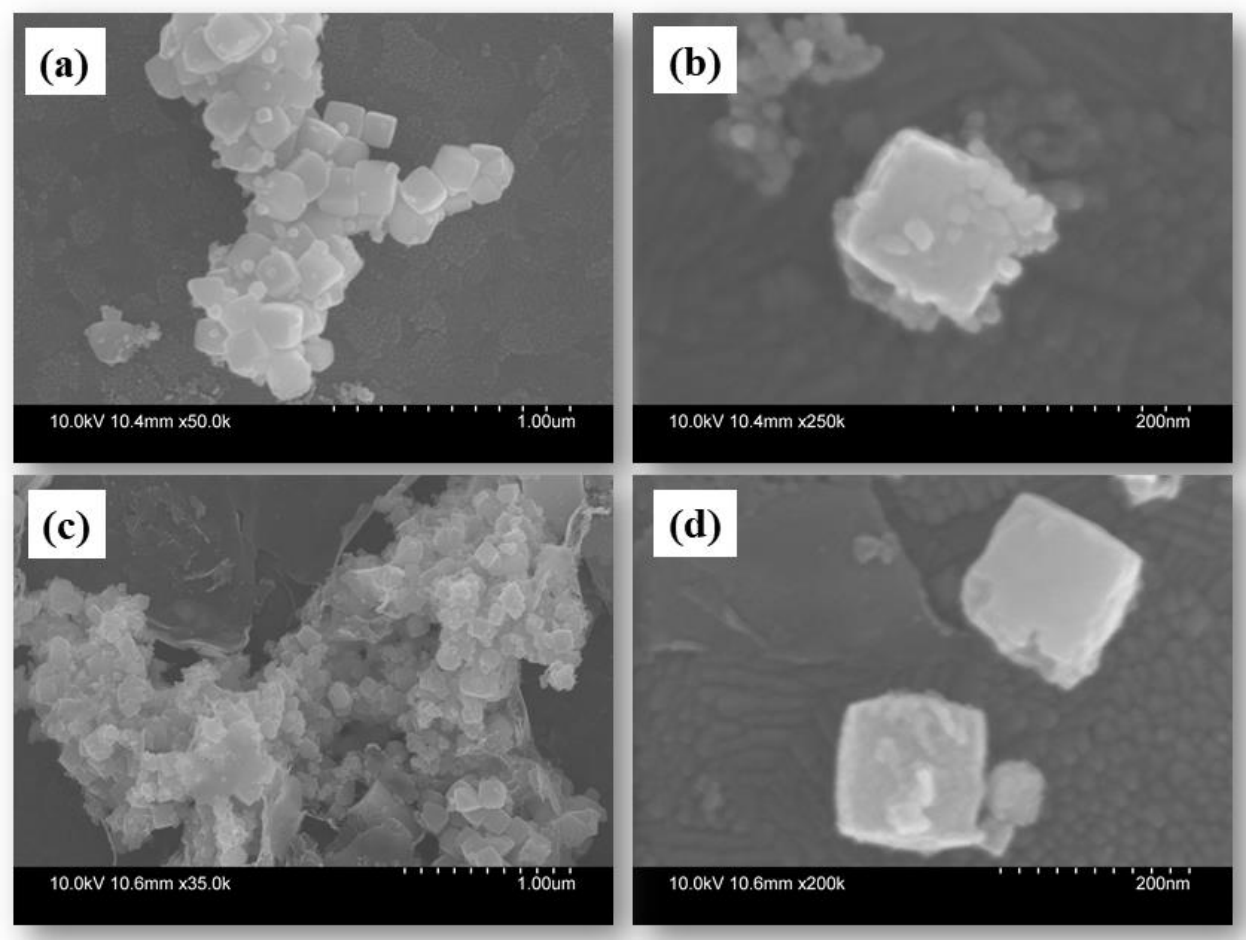

Figure S1. SEM images of ZCO-Air (a, b) and ZCO-Vac (c, d).

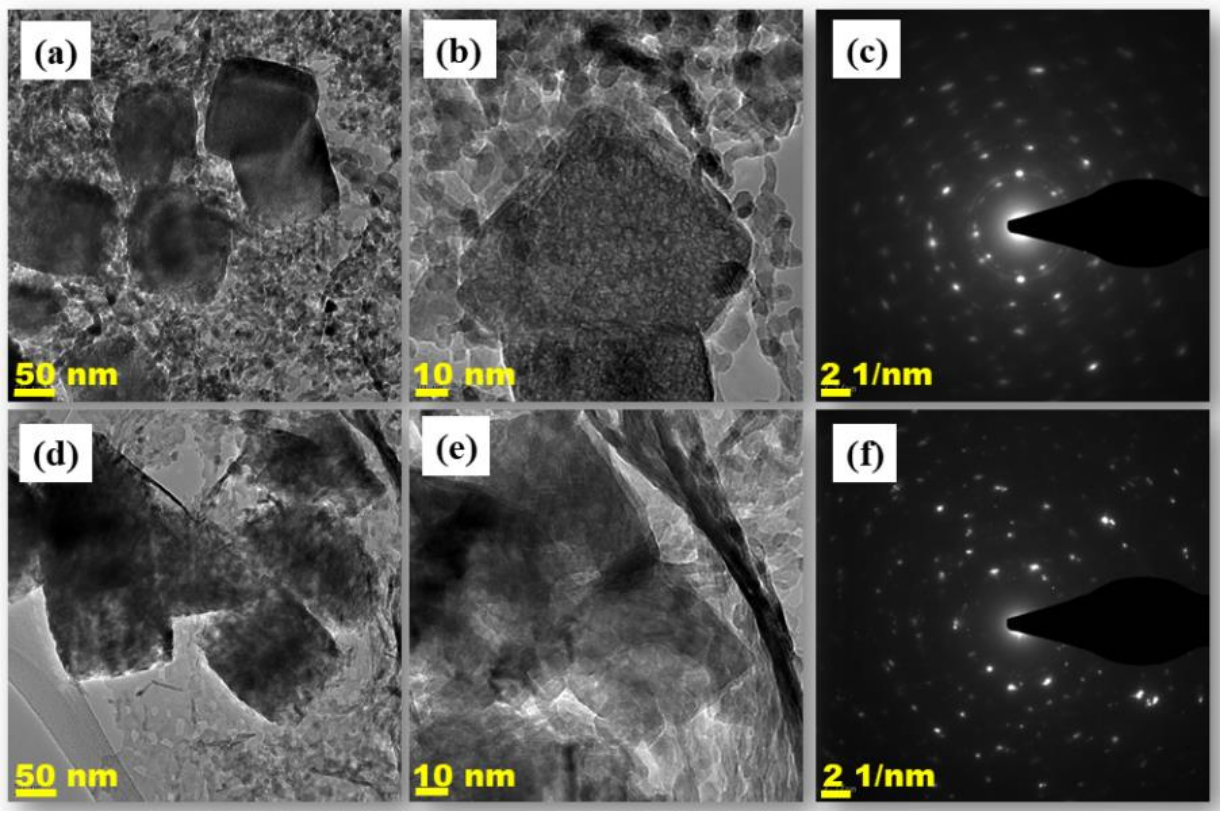

Figure S2. Transmission electron microscopy (a,d), high-resolution transmission electron microscopy (b,e) images, and selected area electron diffraction patterns (c,f) of ZCO-Air (a-c), and ZCO-Vac (d-f).

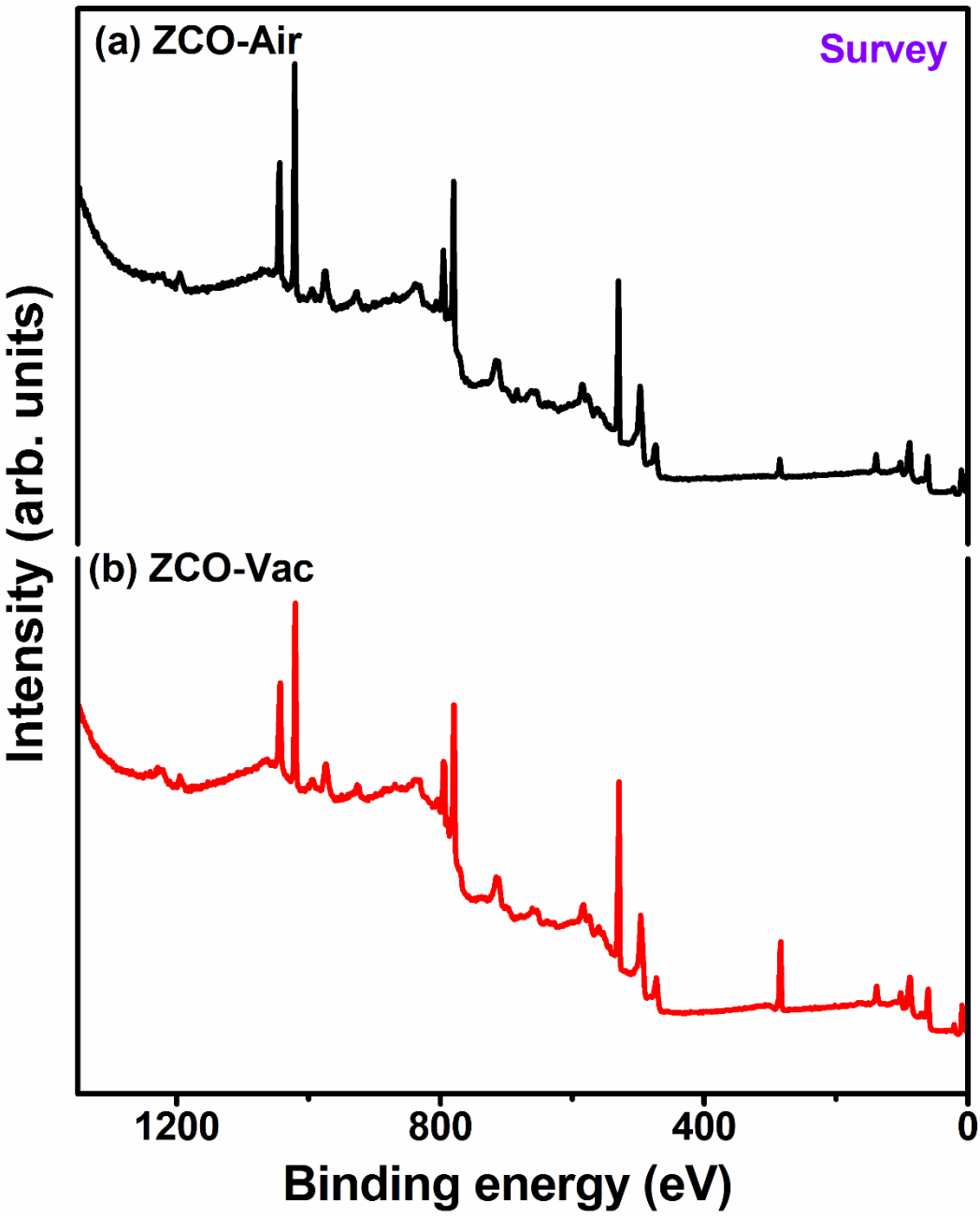

Figure S3. XPS survey spectra of ZCO-Air (a) and ZCO-Vac (b).

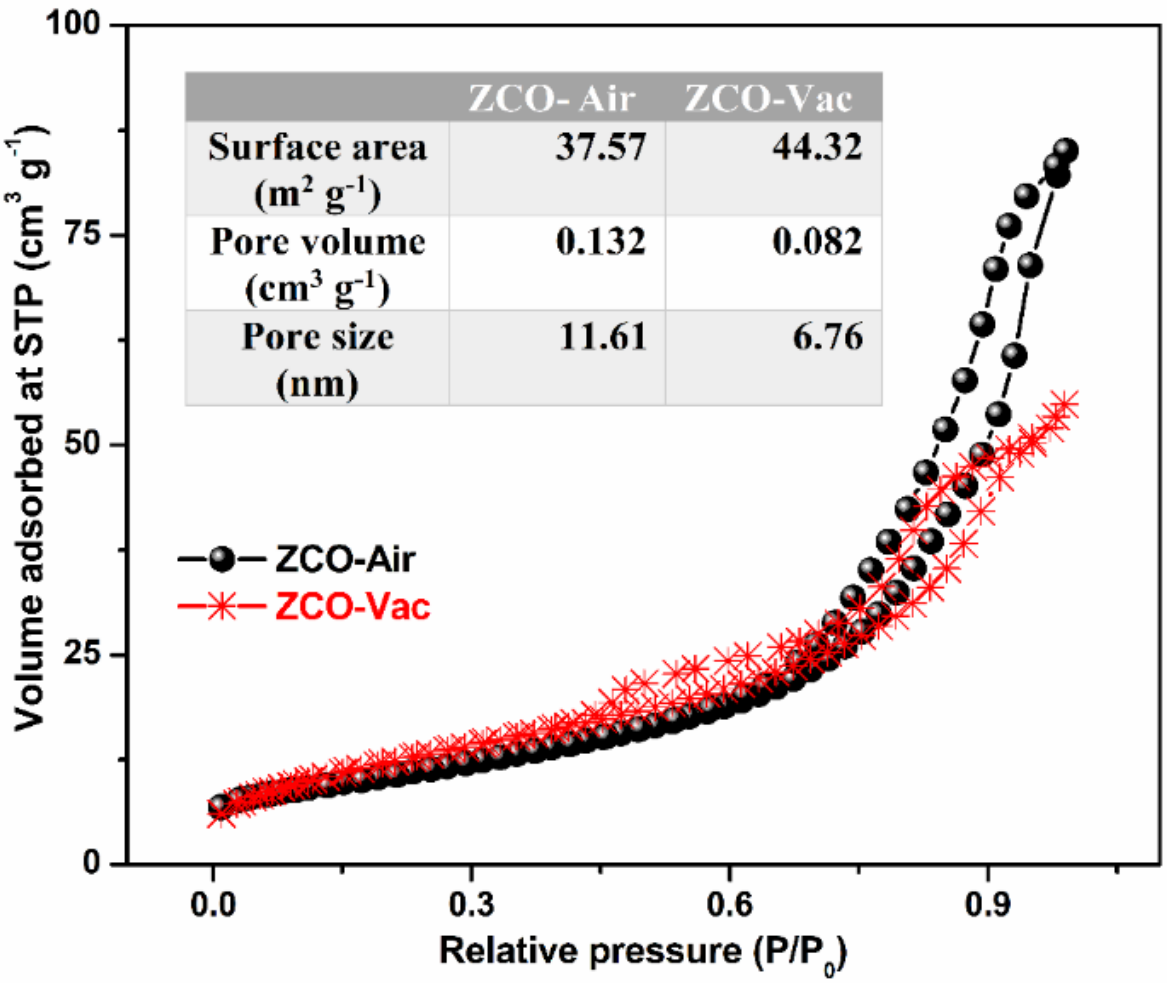

Figure S4. N_2 adsorption and desorption curves of ZCO samples. The inset table lists the parameters of the Brunauer–Emmett–Teller (BET) determined from the respective curves.

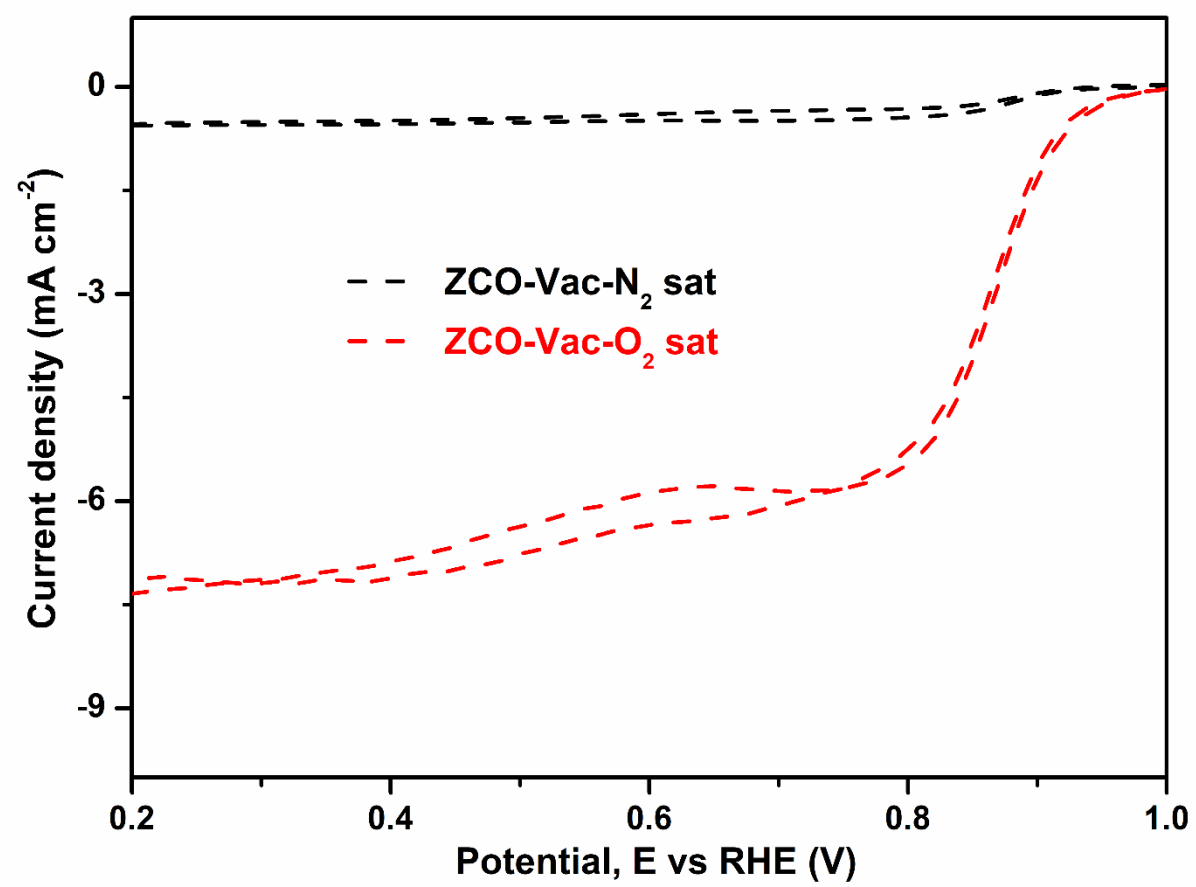

Figure S5. CV of ZCO-Vac in N_2 and O_2-saturated 0.1 M KOH at 1600 rpm with a scan rate of 10 mV s^{-1}.

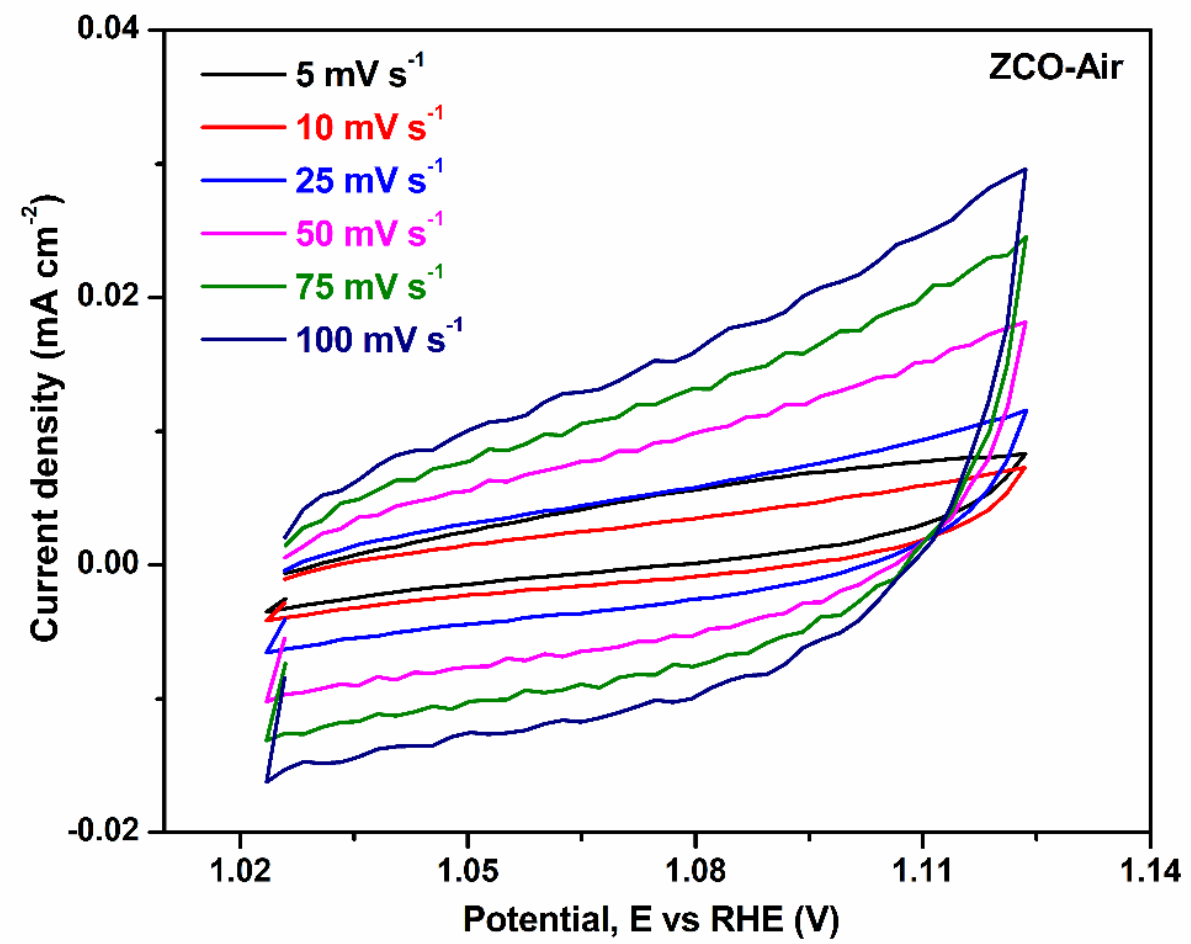

Figure S6. CV of ZCO-Air at different scan rates in N_2-saturated 0.1 M KOH.

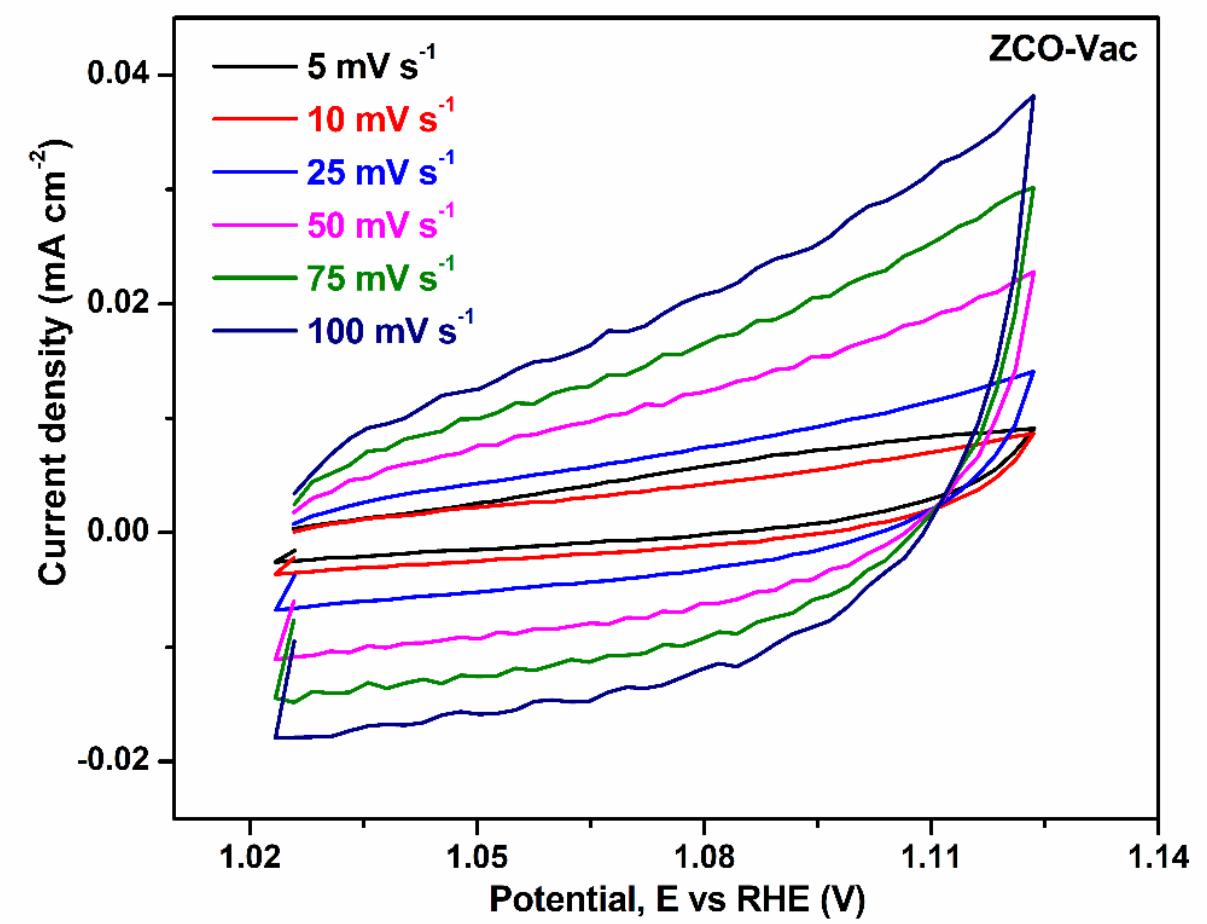

Figure S7. CV of ZCO-Vac at different scan rates in N_2-saturated 0.1 M KOH.

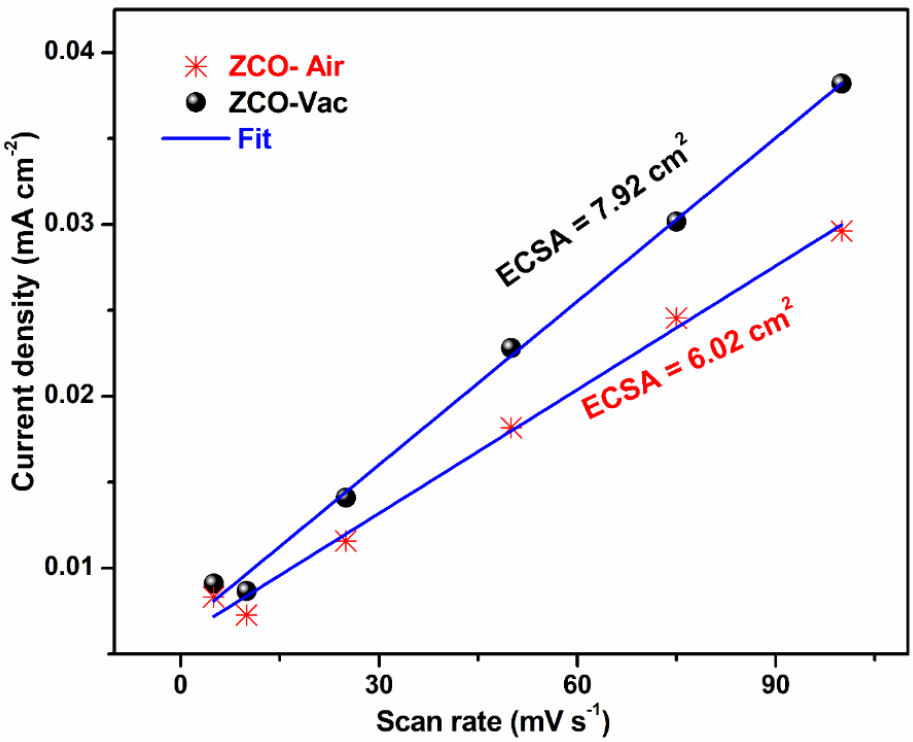

Figure S8. Comparison plots of current density versus scan rates for the electrocatalysts.

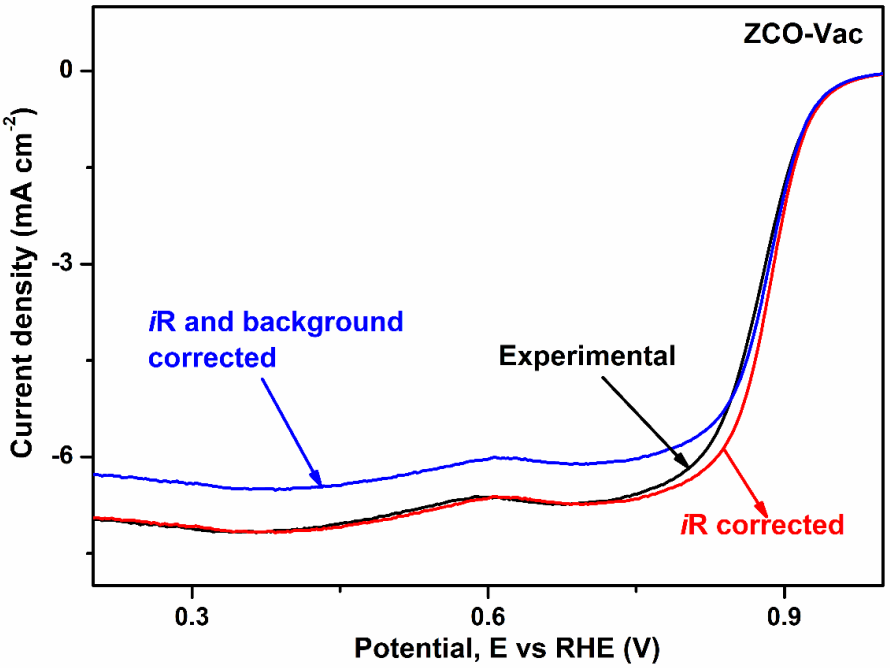

Figure S9. Experimental, *iR*-, and background-corrected linear sweep voltammetry (LSV) curves of the ZCO-Vac sample in O_2-saturated 0.1 M KOH at a rotation rate of 1600 rpm with a scan rate of 10 mV s^{-1}.

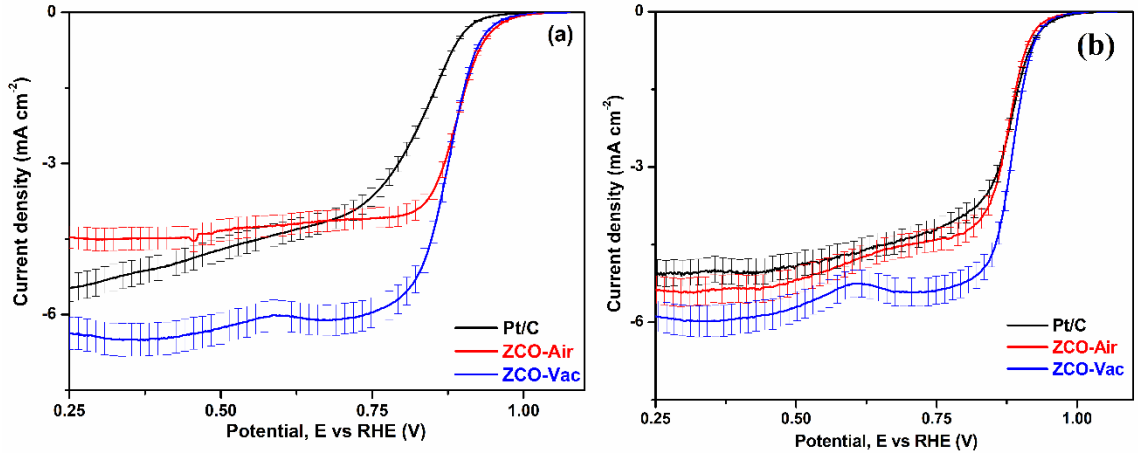

Figure S10. ORR LSV curves (*iR* and background corrected) of ZCO-Air, ZCO-Vac, and Pt/C were measured using (a) graphite rod and (b) Pt counter electrodes at a rotation rate of 1600 rpm with a scan rate of 10 mV s^{-1}.

ORR measurements were performed and compared using the graphite rod (**Figure S10a**) and Pt (**Figure S10b**) as counter electrodes. With graphite rod, the ZCO-Vac and ZCO-Air samples show ORR half-wave potential ($E_{1/2\ (-3\ mA/cm^2)}$) of 0.88 and 0.85 V, respectively. While with Pt, the corresponding values are 0.89 and 0.87 V. Thus, the ORR activity measured with both counter electrodes shows marginal variations. Further, the graphite rod counter electrode was used over Pt to avoid the possibility of the dissolution of Pt and deposition onto the working electrode during the ORR process.

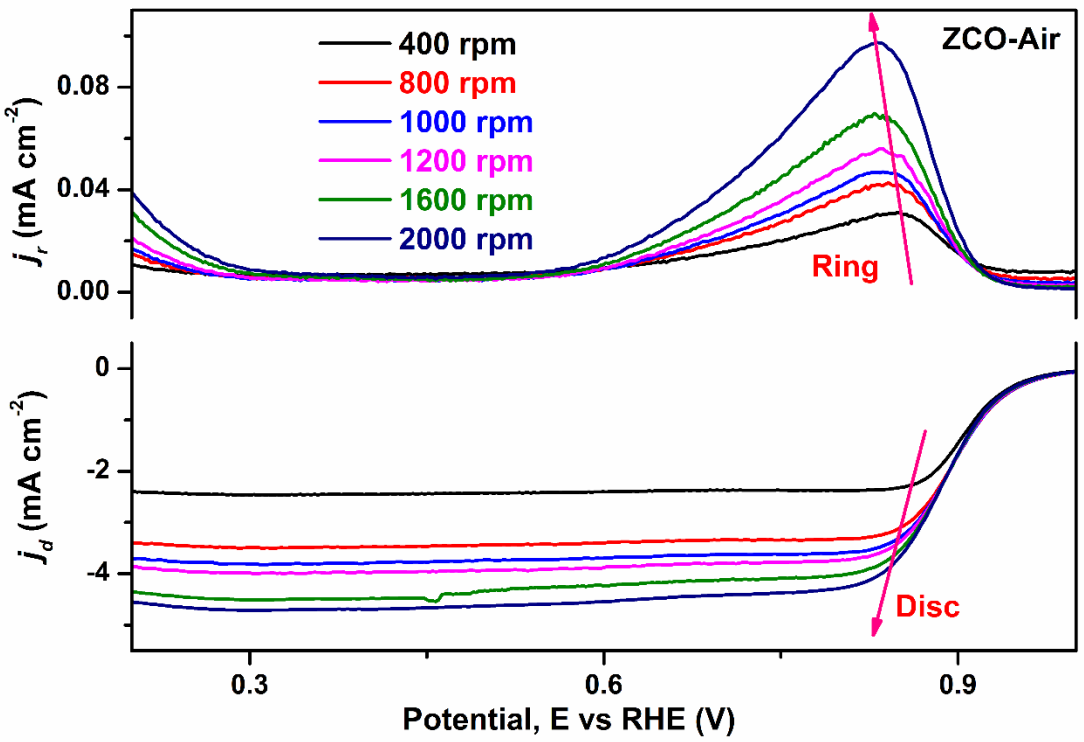

Figure S11. LSV curves of the disc (bottom curves) and ring (top curves) electrodes of the catalytic ORR process of the ZCO-Air in O_2-saturated 0.1 M KOH at different rotation rates with a scan rate of 10 mV s^{-1}.

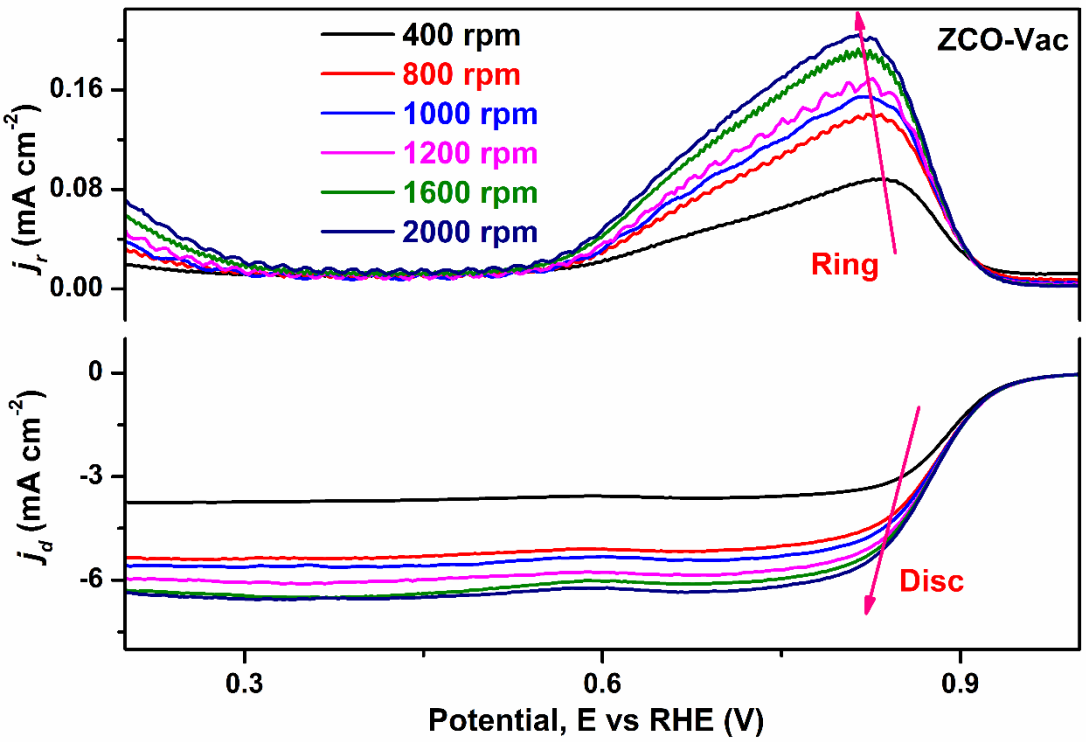

Figure S12. LSV curves of the disc (bottom curves) and ring (top curves) electrodes of the catalytic ORR process of the ZCO-Vac in O_2-saturated 0.1 M KOH at different rotation rates with a scan rate of 10 mV s^{-1}.

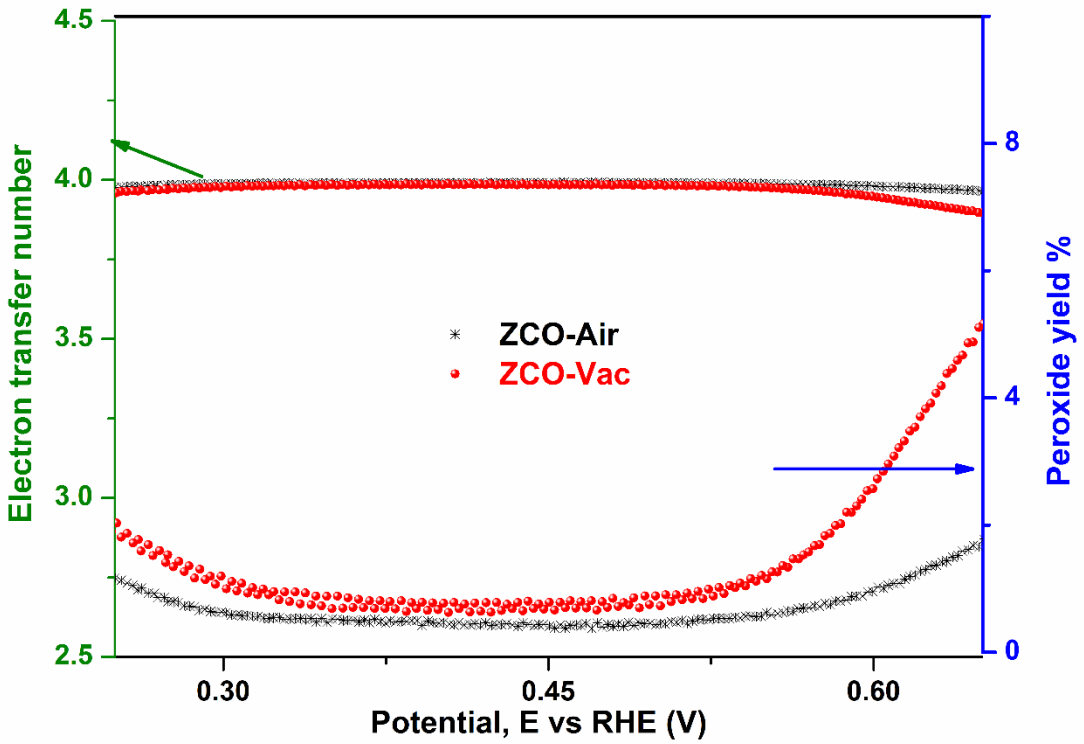

Figure S13. The electron transfer number and peroxide (H_2O_2) yield % of the ZCO samples were calculated using RRDE data in O_2-saturated 0.1 M KOH at 1600 rpm with a scan rate of 10 mV s^{-1}.

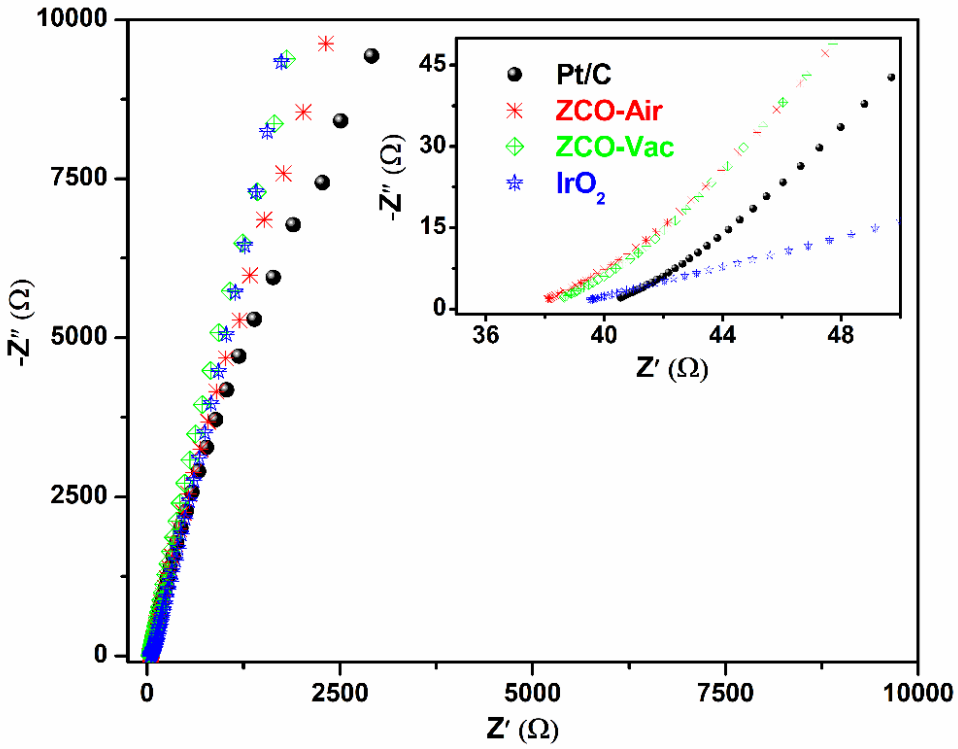

Figure S14. Comparison of impedance spectra of ZCO samples (red and green symbols) with Pt/C (black spheres) and IrO_2 (blue stars) standards in N_2-saturated 0.1 M KOH. The inset shows a magnified view of the data.

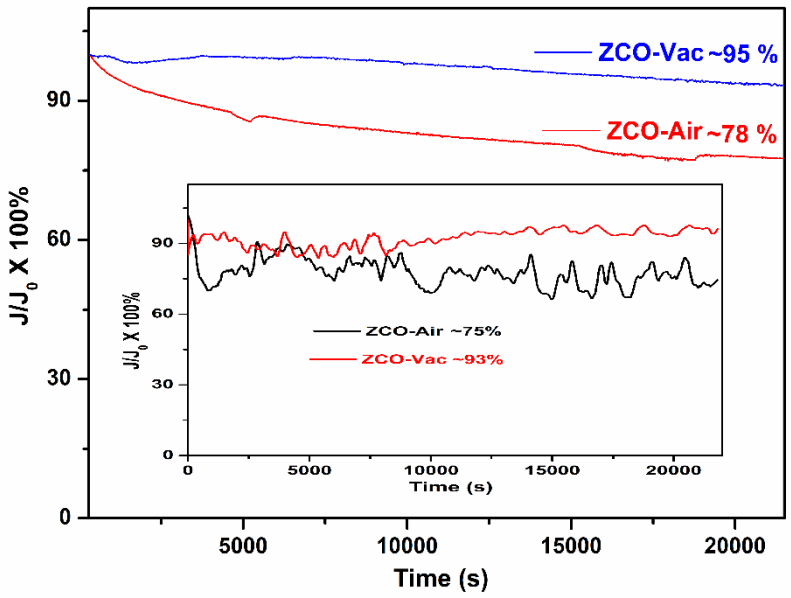

Figure S15. Chronoamperometry of both ZCO samples at 0.45 V vs. RHE for ORR up to 6 h. Inset shows the comparison of the CA of OER for the catalysts at their overpotentials up to 6 h.

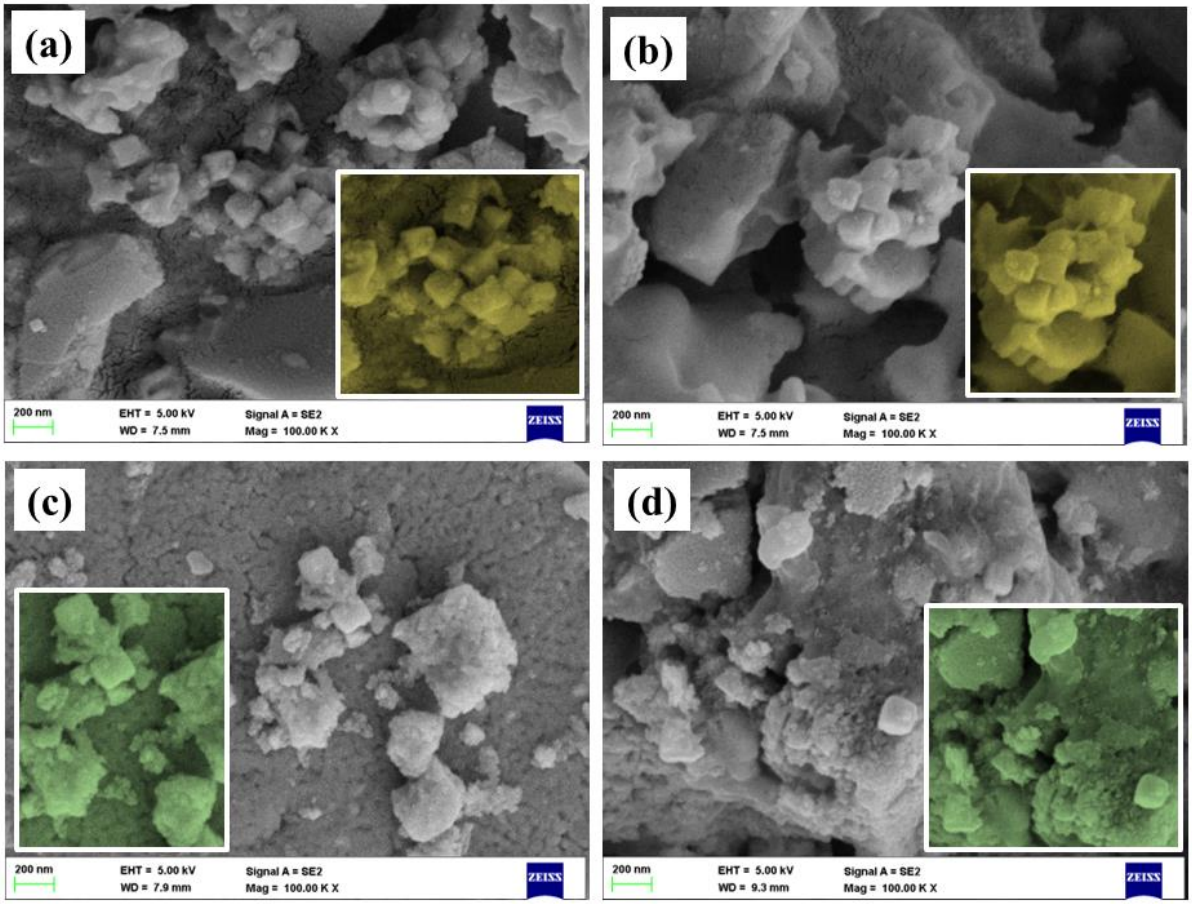

Figure S16. SEM images after CA of ZCO-Air (a,b) and ZCO-Vac (c,d). Insets show the magnified views of the nanocubes of the respective samples.

Enumerating Defective Configurations for Density Functional Theory Calculations

The conventional unit cell of $ZnCo_2O_4$ (ZCO) contains 8 Zn, 16 Co, and 32 O atoms. To precisely model the air-annealed (ZCO-Air) and vacuum-annealed (ZCO-Vac) compositions, while keeping our computational costs tractable, we created a set of supercells with compositions indicated in **Table S1**. We ensured that the compositions we modeled matched the experimental compositions (as obtained from X-ray diffraction measurements, **Table 1** in the main text) as closely as computationally possible. Thus, the ZCO-Vac structural model required the introduction of three Zn vacancies and seven O vacancies within a $2 \times 1 \times 1$ supercell of bulk-ZCO. In comparison, the Zn-Air model required the addition of one Zn vacancy and three O vacancies in a larger $2 \times 2 \times 1$ supercell.

Table S1: Structural models employed for defective ZCO calculations.

Sample	Supercell used	Model composition	Experimental composition
ZCO-Vac	$2 \times 1 \times 1$	$Zn_{13}Co_{32}O_{57}$ ($Zn_{6.5}Co_{16}O_{28.5}$)	$Zn_{6.52}Co_{16.00}O_{28.66}$
ZCO-Air	$2 \times 2 \times 1$	$Zn_{31}Co_{64}O_{125}$ ($Zn_{7.75}Co_{16}O_{31.25}$)	$Zn_{7.78}Co_{16.00}O_{31.29}$

Given the choice of structural models in Table S1, the configurational space between these defects within the supercells created for ZCO-Vac and ZCO-Air is immense. For example, the introduction of Zn and O vacancies can, in theory, lead to $\binom{16}{3} \times \binom{64}{7} \approx 3.5 \times 10^{11}$ configurations within the supercell (the real number of symmetrically distinct combinations is likely to be orders of magnitude lower but still in the realm of computational intractability). Hence, to ensure that we can get a reliable estimate of the electronic density of states (DOS) for both defective structures while keeping the unique configurations that need to be calculated "small", we developed workflows as shown in **Figures S17** and **S18**. Both workflows involved the use of the pymatgen library.

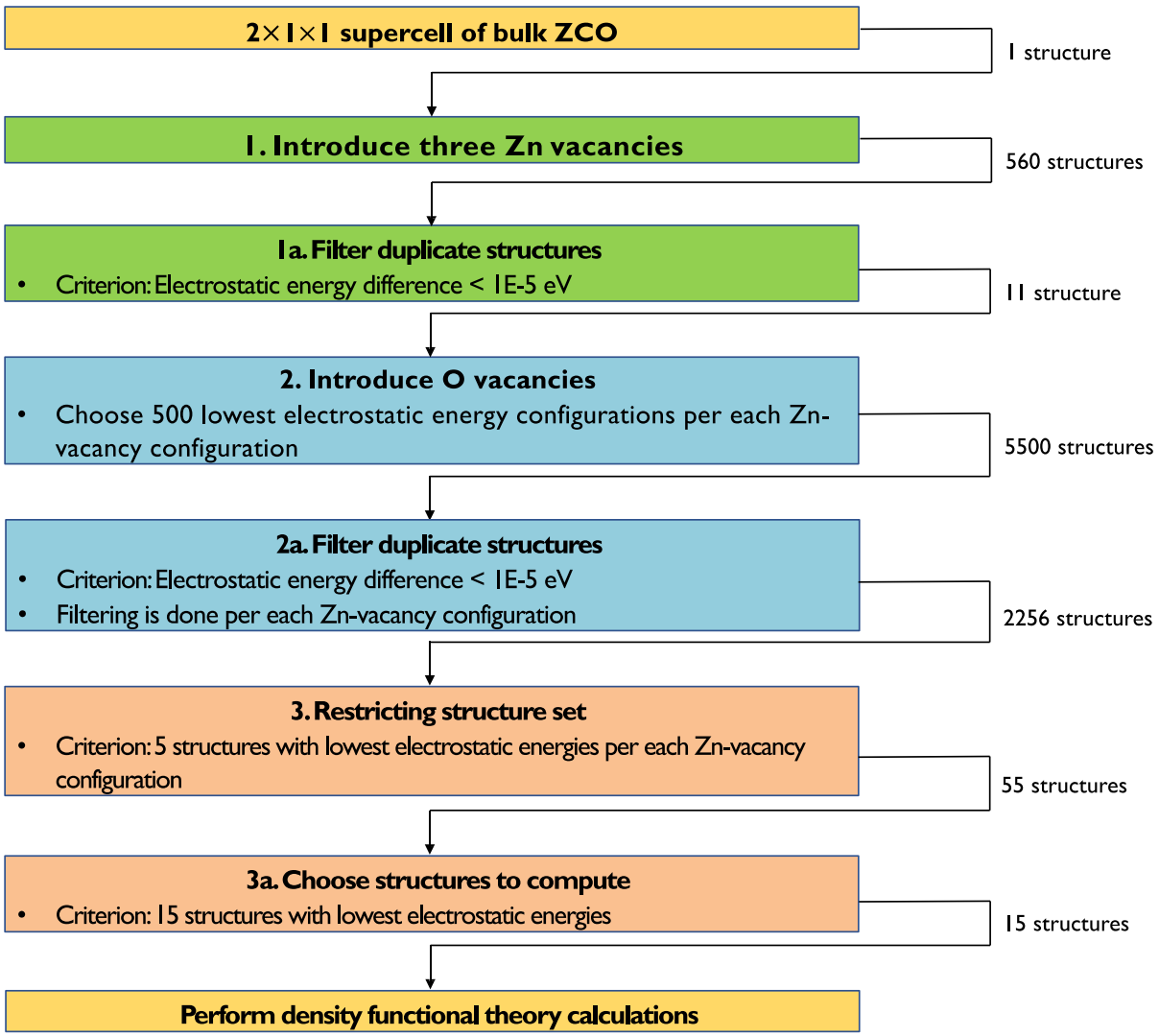

Figure S17. Workflow for performing density functional theory calculations in the ZCO-Vac structural model.

Figure S17 shows the workflow used for enumerating a list of 15 defective structures for the ZCO-Vac structural model, for which we performed density functional theory calculations (as detailed in **Section 2.5** of the main text). After creating a $2 \times 1 \times 1$ supercell of the relaxed bulk ZCO, we first introduced three Zn vacancies (using the "OrderDisorderedStructureTransformation" class of pymatgen),[4] which resulted in a maximum of 560 structures (step 1, green box in **Figure S17**). Subsequently, we used the calculated electrostatic energy (via the Ewald summation technique)[5] to remove Zn-vacancy configurations that were too similar (i.e., exhibited electrostatic energy differences $< 10^{-5}$ eV). Removing such duplicates led to 11 unique structures with three Zn vacancies (step 1a).

For each of the 11 structures, we introduced seven oxygen vacancies and, among the possible configurations, chose the 500 lowest electrostatic energy configurations for each Zn-

vacancy structure, resulting in a total of 5500 structures (step 2). Subsequently, we used a similar electrostatic energy criterion as in step 1 to remove duplicate structures in each set of 500 configurations generated, resulting in 2256 structures across the 11 different Zn-vacancy configurations.

In step 3, we took the electrostatically-distinct oxygen vacancy configurations for each of the 11 Zn-vacancy configurations and chose only the five lowest energy configurations in each set, resulting in 55 structures. Finally, we created a shared pool of 55 structures, ordered them via their electrostatic energies, and chose the 15 lowest energy configurations to perform density functional theory calculations. Out of these 15 structures, we calculated the DOS for the density functional theory-calculated lowest energy configuration, plotted in **Figure 6c** of the main text.

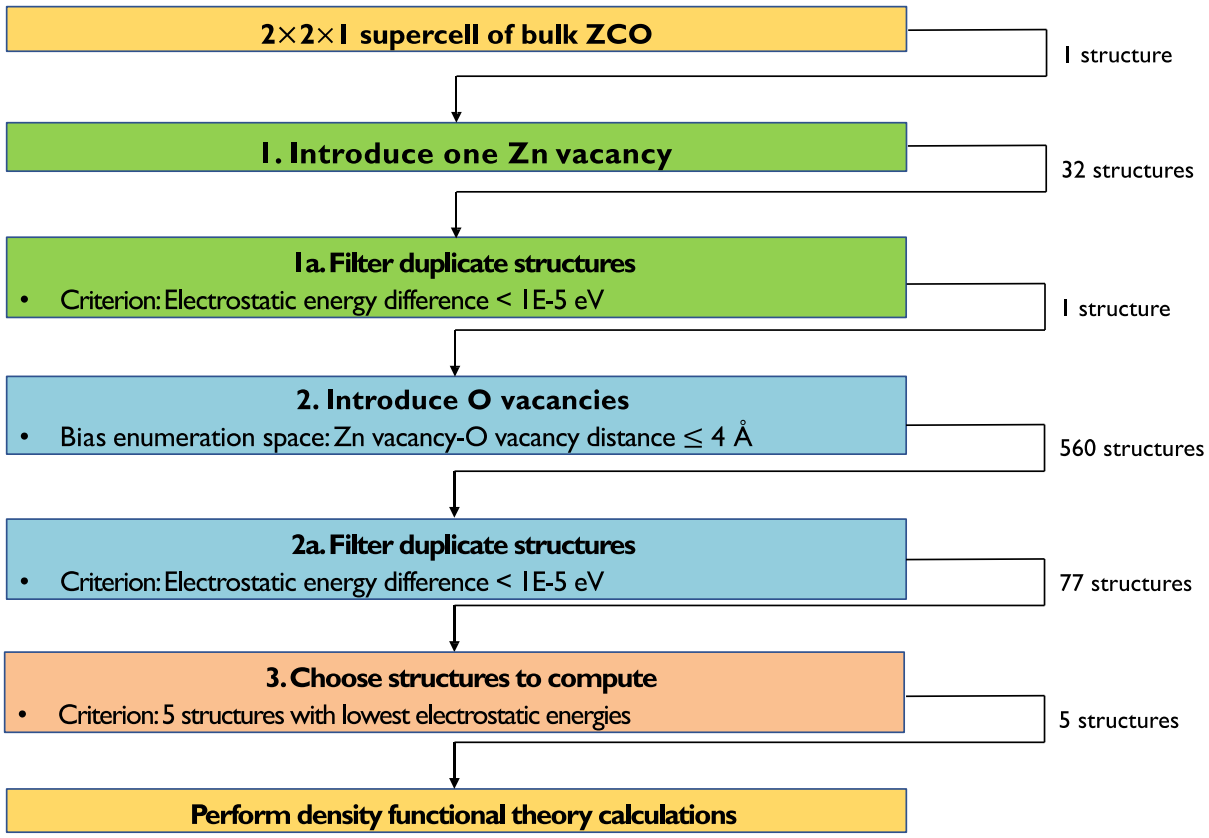

Figure S18. Workflow for performing density functional theory calculations in the ZCO-Air structural model.

To calculate the DOS for the ZCO-Air model, we used a workflow similar to the one used for ZCO-Vac (**Figure S17**), as shown in **Figure S18**. The critical difference between the ZCO-Vac and ZCO-Air structural models is the number of atoms in the supercell (102 and 220,

respectively), which plays the main computational bottleneck in performing density functional theory calculations across the two defective compositions. In the case of ZCO-Air, after introducing a Zn-vacancy in a $2 \times 2 \times 1$ supercell of ZCO, we found only one electrostatically-distinct configuration, as indicated by step 1 in **Figure S18**.

Subsequently, we introduced three oxygen vacancies within the Zn-vacant structure in a biased manner, i.e., we considered oxygen atoms at a distance of $\leq$4 Å from the Zn-vacancy to be removed. The rationale behind this bias is driven by electrostatics: a Zn-vacancy represents holes while an O-vacancy represents electrons, and thus, the two defects must attract electrostatically. Note that O-vacancies also repel electrostatically, which motivated us to choose a 4 Å distance cut-off from the Zn-vacancy, representing the next-nearest-neighbor shell. Thus, introducing the three oxygen vacancies and removing duplicates resulted in 77 structures (step 2). Finally, among the 77 structures, we chose the five electrostatically lowest energy configurations for performing density functional theory calculations (step 3), with the DOS calculated for the density functional theory-calculated lowest energy configuration and plotted in **Figure 6b** of the main text.

References

(1) Chakrabarty, S.; Mukherjee, A.; Su, W.-N.; Basu, S. Improved Bi-Functional ORR and OER Catalytic Activity of Reduced Graphene Oxide Supported $ZnCo_2O_4$ Microsphere. *International Journal of Hydrogen Energy* **2019**, *44* (3), 1565–1578.

(2) Zhou, R.; Zheng, Y.; Jaroniec, M.; Qiao, S.-Z. Determination of the Electron Transfer Number for the Oxygen Reduction Reaction: From Theory to Experiment. *ACS Catalysis* **2016**, *6* (7), 4720–4728.

(3) Fink, M. F.; Eckhardt, J.; Khadke, P.; Gerdes, T.; Roth, C. Bifunctional α -MnO_2 and Co_3O_4 Catalyst for Oxygen Electrocatalysis in Alkaline Solution. *ChemElectroChem* **2020**, *7* (23), 4822–4836.

(4) Ong, S. P.; Richards, W. D.; Jain, A.; Hautier, G.; Kocher, M.; Cholia, S.; Gunter, D.; Chevrier, V. L.; Persson, K. A.; Ceder, G. Python Materials Genomics (Pymatgen): A Robust, Open-Source Python Library for Materials Analysis. *Computational Materials Science* **2013**, *68*, 314–319.

(5) Ewald, P. P. Die Berechnung Optischer Und Elektrostatischer Gitterpotentiale. *Ann Phys* **1921**, *369* (3), 253–287.